Spin transport and superconductivity in half-metallic nanowires and junctions

Yao, J.

2

Fundamental Concepts

2.1. Ferromagnetism

The concepts needed for this thesis in the area of ferromagnetism are a general description, the concept of domains and domain walls, of magnetization dynamics, a note on micromagnetic simulations, and a description of the halfmetallic ferromagnet $La_{0.7}Sr_{0.3}MnO_3$.

2.1.1. General description

A ferromagnet consists of an ordered ensemble of microscopic magnetic moments of electrons. An electron has an intrinsic spin, with a spin angular momentum ($\vec{S}$) attached to it. When the electrons are localized, the orbital angular momentum ($\vec{L}$) also carries a magnetic moment. For such an electron, the magnetic moments are given by:

$$\mu_s = \frac{g_s \mu_B \vec{S}}{\hbar} \tag{2.1}$$

$$\mu_\ell = \frac{g_\ell \mu_B \vec{L}}{\hbar} \tag{2.2}$$

respectively, where g_s is roughly 2 in quantum field theory, $g_\ell = 1$, and $\mu_B = e\hbar/2m_e$. $|\vec{S}| = \hbar/2$, and $|\vec{L}|$ is quantized in multiples of $\hbar$.[1] Due to the orbital motion of a spinning electron, a magnetic field (B) is produced and acts on the magnetic moment of the electron, resulting in angular transfer between $\vec{S}$ and $\vec{L}$, the so-called spin-orbital interaction (SOI), which is described as:

$$H_{s-o} \propto \vec{S} \cdot \vec{L} \tag{2.3}$$

Without dipole or exchange interactions, the system can acquire a net magnetic moment by applying a magnetic field that aligns the moments along the field direction through the Zeeman interaction.
For a system with itinerant electrons, the only source of magnetism comes from the spins. Again, in a non-interacting system of spins, a net magnetic moment occurs in an applied field. The Zeeman interaction populates one spin direction ('spin-up') at the expense of the other ('spin-down'), resulting in a magnetic moment that is proportional to the difference the number of spin-up and spin-down electrons: $M \propto (n_\uparrow - n_\downarrow)$. Also for itinerant electrons, their motion in the electric field of the nuclei gives rise to spin-orbit coupling. SOI yields a variety of intriguing magnetic phenomena, *i.e.* magnetocrystalline anisotropy, spin Hall effect, anisotropic magnetoresistance, *etc.*, and has therefore drawn much attention over time [15–21].

[1] The spin quantum number s is 1/2. The orbital quantum number ℓ can be 0, 1, 2, 3, corresponding to s, p, d, and f wave functions.

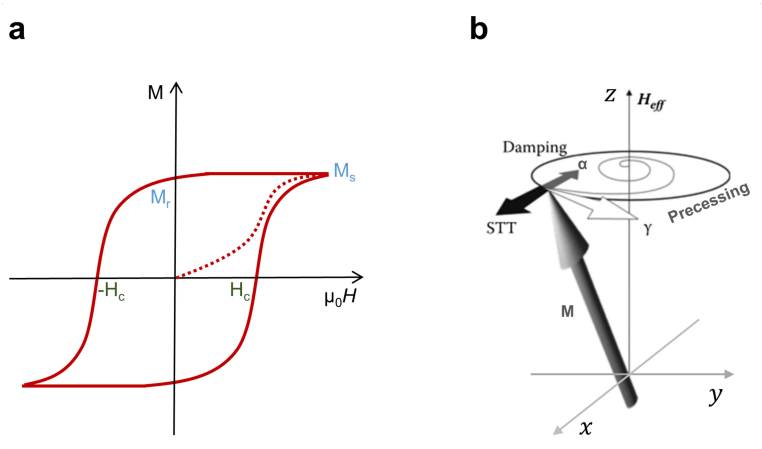

Figure 2.1: Schematic illustration of characteristics of a ferromagnet. (a) A plot of magnetic hysteresis. Starting from a domain state with zero net magnetization M, a saturated magnetization is reached at a high field, as represented by the dotted line. Removing the applied field, the magnet still has a remanent magnetization M_r when zero applied field is reached. Zero magnetization appears at the coercive field ($\pm H_c$). (b) Spin dynamics with the applied field and electric current. H_{eff} points to the direction of z axis. M rotates about the z axis in a spiral trajectory and eventually align with H_{eff}, as a consequence of damping and STT. Images adapted from Ref. [22].

Magnetic moments, either localized or itinerant, can order spontaneously through dipole and exchange interactions. The simplest type is ferromagnetic order, where all moments point in the same direction. When systems contain moments with different magnitudes, the order is called ferrimagnetic. When the order is more complicated and moments point in different, even opposite, directions, it is called antiferromagnetic. The dipole interaction is a good example of an interaction that is antiferromagnetic in nature. For ferromagnets, long-range order sets in below the Curie temperature T_c, roughly speaking the temperature at which the exchange interaction between either localized or itinerant electrons $-2j\vec{S}_i \cdot \vec{S}_j$, with j the strength of the interaction and thermal energy ($k_B T$) are of comparable magnitude. The exchange interaction is a consequence of the Coulomb repulsion and the Pauli exclusion principle and can have a strength of the order of Tesla's or more. Above T_c, thermal fluctuations break the ordered arrangement of magnetic moments, leading to the breaking up of the ferromagnetic state.

2.1.2. Magnetic domains and domain walls

In a bulk material with a certain shape, the magnetic state is often not uniform. Energetically, the system strives to minimize stray fields leaking into the vacuum, by forming domains with different directions of their magnetization. A simple example

is given in Fig. 2.1a, showing domains as they can be expected in a square-shaped ferromagnetic thin film. Note that the net macroscopic magnetic moment of this object is zero. There is energy cost involved in domain formation, residing in the domain walls (DW) that separate the domains. Domain formation is a quite complicated phenomenon since the domain structure comes from an often delicate balance between exchange interactions, magnetocrystalline anisotropy, and shape anisotropy. Fortunately, present-day computing power for performing micromagnetic simulations of magnetic structures goes a long way to understand domain structure in actual experimental devices, as will be discussed below. A consequence of the domain structure is that the process of magnetization and demagnetization of a ferromagnet with a magnetic field H_a is hysteretic. Fig. 2.1b schematically depicts the behavior of $M(H_a)$. Increasing H_a from the virgin ($M = 0$) state removes aligns domains, and M increases until the saturated magnetization (M_s) is reached. When decreasing the field, domains start to form again, depending on the detailed energy balance. Usually, the zero-field magnetization is non-zero and called the remanent magnetization M_r. Zero moment is reached at the coercive field H_c, and saturation magnetization again at large negative H_a. Increasing the field traces out the loop shown in Fig. 2.1.

Magnetic domain walls (DWs) have been extensively studied during the last decades: magnetization reversal, used in all sorts of magnetic memory devices from magnetic tapes onwards, depends on domain wall motion. Also in the next generation of spintronic devices, the key challenge lies in the creation and manipulation of DWs [23, 24]. Randomly-arranged DWs in bulk material offer no practical application in spintronics, but on the nanoscale, shape anisotropy appears to be quite powerful to tailor DWs. For instance, constricting nanostructured ferromagnets can introduce a local barrier that acts as a pinning site for a DW and constitute a logical zero (absence) or 1 (presence). Also, prototype devices have been developed in which injection and moving DWs in nanowires are the carriers of information, the so-called racetrack memory [25], which can greatly increase the data storage density and operation speed.

Conventionally, DW motion is driven by a magnetic field or a (spin-polarized) electric current. The dynamics of DW motion are governed by the Landau-Lifshitz-Gilbert (LLG) equation [26]:

$$\frac{dM}{dt} = -\gamma M \times H_{eff} + \frac{\alpha}{M_S}\left(M \times \frac{dM}{dt}\right) \tag{2.4}$$

where M is the local magnetization, H_{eff} is the sum of the external field and local anisotropy and demagnetization field, $M_S = |M|$, $\gamma = -e/m_e$ is the gyromagnetic ratio, and α is the Gilbert damping constant. The first and second terms on the righthand side of Eq. 2.4 describe the spin dynamics with H_{eff}, *i.e.* spin precession and damping. As demonstrated in Fig. 2.1c, the H_{eff} points along the z axis. Spin hence precesses about z axis in a spiral path at the Larmor frequency ($\omega_L = \gamma B$). In the process,

analyzing the components of M gives:

$$\frac{dM_z}{dt} = \gamma (M \times B)_z \frac{M - M_z}{T_1} \tag{2.5}$$

$$\frac{dM_x}{dt} = \gamma (M \times B)_x \frac{M_x}{T_2} \tag{2.6}$$

$$\frac{dM_y}{dt} = \gamma (M \times B)_y \frac{M_y}{T_2} \tag{2.7}$$

where T_1 is the longitudinal relaxation time (relaxation back to the $z-$axis), and T_2 is the transverse relaxation time, taking place in the $xy-$plane. M_x and M_y eventually become zero at the equilibrium state of M, as a consequence of the damping. Spin damping makes M and H_{eff} parallel and leads to the DW motion. Note that, if $\alpha = 0$, moments in the DW will only rotate without moving. In addition to α, an intrinsic inertial relaxation of spin angular momentum is observed experimentally at a frequency of ~0.5 THz and yields an extra time derivative term $\tau d^2M/dt^2$ [27]. Such ultrafast spin dynamics may pave an avenue toward next-generation high-speed magnetic sensors and spintronics.

The effects of electric current on the spin dynamics are captured as additional terms in the LLG Eq. 2.4, the so-called adiabatic and non-adiabatic spin torque transfer terms (STT). For a spin-polarized charge current j_e along the x direction of a ferromagnetic nanowire, that leads to

$$\frac{dM}{dt} = -\gamma M \times H_{eff} + \frac{\alpha}{M_S}\left(M \times \frac{dM}{dt}\right) - \frac{b_J}{M_s^2} M \times \left(M \times \frac{dM}{dx}\right) - \frac{c_J}{M_s} M \times \frac{dM}{dx} \tag{2.8}$$

where $b_J = P j_e \mu_B / eM_s(1+\xi^2)$, $c_J = P j_e \mu_B \xi / eM_s(1+\xi^2)$. Both c_J and b_J have the units of velocity. $c_J/b_J = \xi \approx 10^{-2}$ [26]. In essence, ξ is the ratio of characteristic time for exchange interaction and spin-flip rate and represents the degree of non-adiabaticity of the STT. P is the spin polarization of the applied current. The equation describes how the spin angular momentum is transferred to the local spins of the DW, giving rise to DW motion. In reality, the situation is more complicated. The adiabatic STT generally *assists* DW motion. If the adiabatic STT is aligned with the damping torque, M tends to reach the equilibrium rapidly, *i.e.* DW motion is accelerated. If, however, the adiabatic STT is opposite to the damping torque, the DW begins to revolve away from H_{eff} with a steady increase of precession angle. Besides, once the external stimuli stop, *i.e.* H_{eff}, and spin-polarized currents, the DW may be driven back to the initial position by the non-adiabatic STT. The non-adiabatic STT arises from the anisotropy and demagnetization fields and exerts torque on the spins of the DW, affecting the DW motion independently. To maximize the STT, the applied currents should be high-density ($\sim 10^{12}$ A/m^2). Unfortunately, such high-density currents inevitably generate Joule heating and hinder the performance of relevant spintronics. According to the third and fourth terms in Eq. 2.8, increasing P is an alternative way, meaning highly-spin-polarized soft ferromagnets are appropriate candidates.

2.1.3. Micromagnetic simulation

As already mentioned, understanding the magnetization dynamics of a ferromagnet is of importance in the field of spintronics research. For this work, it is important to understand and control domains, and in general the spin texture of the ferromagnetic layers in the devices we want to research. For this we use simulation software to calculate magnetization configurations and dynamics. In particular, we employ the GPU-accelerated mumax3 program to model the magnetization dynamics microscopically [28]. In the microscopic simulation, several materials parameters should be considered: the exchange stiffness A_{ex}, the anisotropy constants K_u for uniaxial anisotropy and K_c for biaxial anisotropy, and the saturation magnetization M_s. Then, the exchange length of a ferromagnet can be determined as $\ell_{ex} = \sqrt{2A_{ex}/\mu_0 M_s^2}$. Subdividing the ferromagnetic object into equal-sized grids with uniform magnetization, the time-evolving dynamics of magnetization is simulated by solving the differential Eq. 2.4 numerically. To achieve a real-life situation, the cell size must be smaller than ℓ_{ex}. In each cell, the magnetization consists of three components m_x, m_y, and m_z along the x, y, and z axes. Calculating the norm of the three components yields the averaged value of the magnetization. To speed up the convergence of the microscopic simulation, the damping constant α can be set to an artificial value without affecting the outcome [29].

2.1.4. Half-metallic $La_{0.7}Sr_{0.3}MnO_3$

The STT terms in Eq. 2.8 make clear that currents with a high spin polarization are of interest. A P of (close to) 100% is found in halfmetallic ferromagnets such as $La_{0.7}Sr_{0.3}MnO_3$ (LSMO). This doped manganite has been considerably studied during the last decades, exhibiting various intriguing phenomena such as halfmetallicity, colossal magnetoresistance, tunable magnetocrystalline anisotropy, *etc.*, thanks to the spin-orbital-lattice coupling [30, 32, 33]. Fig. 2.2a shows the pseudocubic crystal structure of LSMO unit cell, where a Mn ion sits at the center (B site) and is surrounded by oxygen octahedron, with La/Sr at the corners (A sites). The properties of LSMO are deterministically related to the lattice structure, which is characterized by the tolerance factor $t = (r_A + r_O)/\sqrt{2}(r_B + r_O)$ [34]. r represents the radius of the various elements. For LSMO, due to the radius difference between La/Sr and Mn ($r_{La/Sr} > r_{Mn}$), the oxygen octahedra are tilted, and the bond angle of the Mn-O-Mn chain is ~166.3^o. Therefore, the crystal structure of LSMO is rhombohedral. In the pseudocubic coordinate system, the edge length (a) of the LSMO unit cell is 0.388 nm. To minimize the magnetic and electrical inhomogeneities of LSMO when growing thin films, the substrate we use is $(LaAlO_3)_{0.3}(Sr_2TaAlO_6)_{0.7}$(LSAT) with a = 0.387 nm. The lattice mismatch is about -0.2% in this case, offering negligible clamping strain and correspondingly yielding epitaxial and homogeneous LSMO thin films.

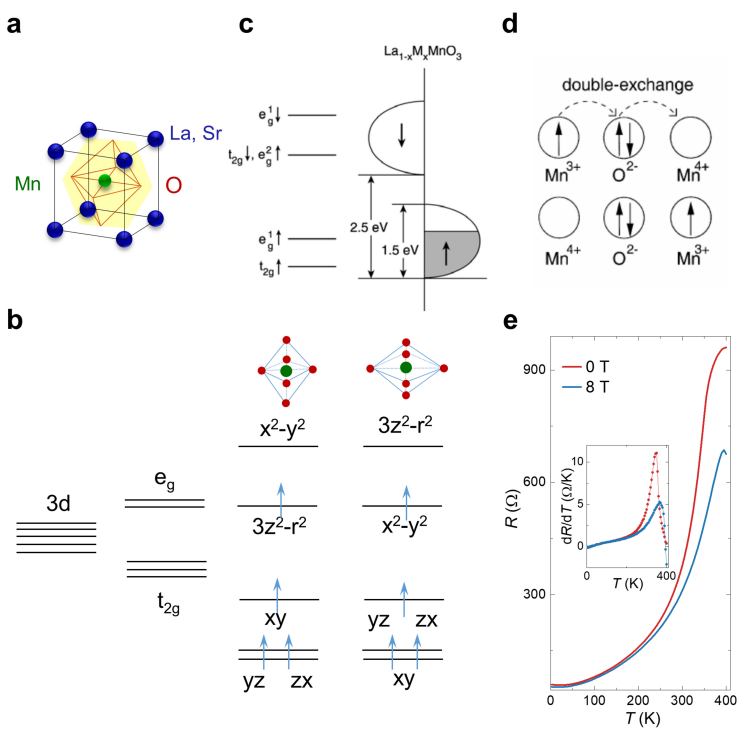

Figure 2.2: Overview of structural, magnetic, and transport properties of LSMO. (a) Sketch of the pseudocubic crystal structure of LSMO unit cell, in which A site is occupied by La/Sr, Mn sits at B site in the oxygen octahedron, leading to the strong orbital hybridization (represented by yellow cloud schematically). (b) In the presence of epitaxial strain, five-fold degenerate 3*d* levels are lifted by crystal field and further by Jahn-Teller distortion. (c) The density of states of LSMO indicates the nature of half-metallic transport, *i.e.* one spin band is conducting while the other is insulating. (d) Illustration of double exchange among Mn^{3+}, O^{2-}, and Mn^{4+}, under the condition of alignment of neighboring spins. (e) Temperature-dependent resistance characteristics of LSMO upon zero field (blue curve) and out-of-plane 8 T (red curve) display the famous colossal magnetoresistance effect. The inset dR/dT vs T demonstrates T_c is shifted to a higher temperature with 8 T. Images adapted from Ref. [30–33].

In the field of spintronics, LSMO is widely used in multiferroic heterostructures, magnetic tunneling junctions, spin-polarized currents generator, *etc.* [35], mainly because of its high spin polarization ($P \sim 96\%$) [22, 36]. Here, we briefly discuss the origin of the ferromagnetism of LSMO and the concurrent halfmetallicity.

As depicted in Fig. 2.2b, the five-fold degenerate 3*d* orbitals are split into e_g and t_{2g} orbitals as a consequence of the ligand crystal field, with $\Delta \sim 1.5$ eV the energy difference between the lowest t_{2g} level and the highest e_g level. The exchange energy E_{ex} is 2.5 eV (see Fig. 2.2c). Growing LSMO on single-crystal substrates introduces either compressive or tensile strain, *i.e.* axial elongation of oxygen octahedra in z or xy plane (Jahn-Teller distortion), resulting in the further splitting of both e_g and t_{2g} orbitals. In

the case of Mn^{3+}, with 4 electrons, Hund's rules dictate that electrons with equal spin first populate the t_{2g} levels, and a single electron fills the e_g orbital, still with the same spin. For Mn^{4+} with 3 electrons, the e_g level remains empty. The magnetic moment is only due to the spin and is, therefore, 4 μ_B for Mn^{3+} and 3 μ_B for Mn^{4+}. Doping the parent compound $LaMnO_3$, where La is trivalent (La^{3+}), with Sr^{2+}, a mixture of Mn^{3+} and Mn^{4+} is created. Given the chemical stoichiometry we use, of 70% La and 30% Sr, the total magnetic moment of a LSMO unit cell is $0.7(4\mu_B) + 0.3(3\mu_B) = 3.7\mu_B$ in theory [37]. The measured saturated magnetic moment of our LSMO thin film grown on LSAT substrates is calculated to be 3.8 $\mu_B/f.u.$. The small discrepancy is probably due to the contribution of orbital angular momenta (μ_ℓ) [38].

The spin-subband structure of LSMO brings out the property of half-metallic transport, which can be understood in the framework of the double-exchange mechanism. As seen in Fig. 2.2d, for $T \ll T_c$, electron hopping between Mn^{3+} and Mn^{4+} is mediated by the middle O^{2-} through the overlap of the d orbital of Mn and the p orbital of O. The prerequisite of electron hopping is the alignment of neighboring spins.[2] As a result, electrons flowing in LSMO are polarized, *i.e.* one spin state yields conducting transport while the other gives insulating behavior. Therefore, electron hopping governs both the ferromagnetic and conducting properties of LSMO, meaning ideally a metal-to-insulator transition occurs coincidentally with a transition of ferromagnetism to paramagnetism ($T_{MI} = T_c$). More interestingly, for T close to T_c, the double exchange interaction is significantly suppressed due to the divergence of the magnetic susceptibility. By applying an external field of the order of Tesla's, neighboring spins can be realigned, enabling electron hopping even at $T \geq T_c$, and leading to the so-called colossal magnetoresistance. Fig. 2.2e demonstrates the temperature-dependent resistance measurements of LSMO with 8 T (blue curve) and without field (red curve). Clearly, the resistance becomes smaller as the field is large enough to recover double exchange interaction and therefore makes LSMO less resistive. Accordingly, T_c increases, as verified in the inset $\mathrm{d}R/\mathrm{d}T$ versus T curves.

The micromagnetic structure of LSMO in thin films is simulated with the GPU-accelerated mumax3 software package by solving the LLG equation [28], in order to get insight into magnetic field control of the spin texture in the LSMO devices. The dimension of such nanostructured LSMO is measured by scanning electron microscopy and split into grids (pixels) in the simulation design of mumax3. The number of grid points should be a power of 2 for the purpose of accelerating the simulation. Notably, the grid size must be comparable to the exchange length (ℓ_{ex}) of LSMO to achieve realistic results. The numbers used are $M_s = 5.75\times10^5$ A/m and $A_{ex} = 1.7\times10^{-12}$ J/m, $\ell_{ex} = \sqrt{2A_{ex}/\mu_0 M_s^2} = 2.86$ nm. Therefore, the grid size is set to 2.5 nm in all the simulations. Moreover, although the magnetocrystalline anisotropy of LSMO is weak, it

[2] The probability of electron hopping is $t_0\cos(\theta/2)$. θ is the angle between spins and determines the magnetic ground states of $La_{1-x}Sr_xMnO_3$.

changes with epitaxial strain and thickness. According to Ref. [39], the anisotropy is uniaxial in a 10 nm LSMO and becomes biaxial in thicker LSMO (20 nm or 40 nm) on LSAT substrate with a miscut angle of $\sim 0.2^o$. Correspondingly, the anisotropy constants K_u and K_c are altered in simulating DWs in notched LSMO nanostructure (Chapter 3) and an LSMO disk (Chapter 5), respectively. In addition, the damping constant α is intentionally set to 0.5 to speed up the convergence of magnetization in the simulation, rather than using experimental values of the order of 10^{-4} [12].

Investigating spin transport in normal-state and superconducting LSMO is our interest in this thesis. As introduced above, LSMO is half-metallic and has a high T_c. In contrast to the conventional ferromagnets, LSMO holds promise to manipulate DW with a lower density of critical current ($\sim 10^8$ A/m^2) and inject the spin-polarized currents efficiently into a normal metal [13, 40]. Moreover, superconducting LSMO carries equal-spin triplet correlations and exhibits intriguing quantum phenomena [14].

2.2. Superconductivity

In the area of superconductivity, also a general description is given, then Josephson effects are generally discussed, including normal metal (N) weak links, then ferromagnets as the weak link, and finally the halfmetal.

2.2.1. Origin of Superconductivity

Superconductivity was discovered in 1911 by Heike Kamerlingh Onnes in Leiden [41]. It is a macroscopic quantum phenomenon. The resistance of a superconductor approaches zero below the critical temperature (T_c), accompanied by the Meissner effect (flux expulsion) in the presence of a magnetic field [42]. The formation of Cooper pairs with opposite spins (*i.e.* singlets)[3] accounts for the onset of superconductivity in conventional low-T_c superconductors, which is described by the BCS theory [43]. In general, electrons experience scattering events above T_c, leading to the electrical resistance and energy dissipation. This process can be simply explained in the two-dimensional k space. The applied voltage moves the Fermi sphere by δk_x along the x direction. Soon, electrons relax to the low energy states, as a consequence of plenty of scattering processes. As a result, current dissipates energy in some way or other. However, below T_c, the scattering processes give rise to no change in the center of mass momentum of paired electrons. Therefore, we see no decay of stationary supercurrent, leading to a zero-resistance state. A theoretical description of superconductivity

[3] Singlets are bosonic-like quasiparticles and obey the Pauli exclusion principle. The possible pairing symmetry will be discussed later.

is given below.

Owing to the phonon-mediated Cooper pairing with a typical strength of 0.01 eV, the size of singlets (ξ_0) usually varies from the order of several nanometers to micrometers, as a result of minimizing the Coulomb repulsion (> 1 eV) at the atomic scale. This means singlets overlap in space and therefore become a collective phenomenon. Consequently, the quantum coherence of singlets can be stated as a macroscopic wave function given by:

$$\Psi(r,t) = \Psi_0(r,t)e^{i\theta(r,t)} \tag{2.9}$$

where r and t represent space and time, respectively, and θ is the gauge-covariant phase. In a simplified picture, the local density of singlet Cooper pairs n_s is equal to $|\Psi(r,t)|^2$, and $n_s = n_e/2$, where n_e is the normal electron density of the material. The most practical way to introduce the basic parameters that describe the properties of the superconducting state is through the well-known Ginzburg-Landau (GL) approach,[4] in which Ψ is a complex order parameter [45]. Two length scales are naturally defined in GL theory. One is the GL coherence length ξ_{GL} which sets the length over which the order parameter can change significantly. The other is the magnetic field penetration depth λ_L (the London penetration depth) that sets the length over which a magnetic field can penetrate into a superconductor. Of practical importance is their temperature dependence, which, not too far from T_c, follows from GL theory as:

$$\xi_{GL}(T) = \frac{\xi_{GL}(0)}{\sqrt{1-\frac{T}{T_c}}} \tag{2.10}$$

$$\lambda_L(T) \approx \frac{\lambda_L(0)}{\sqrt{1-(\frac{T}{T_c})^4}} \tag{2.11}$$

where $\xi_{GL}(0) = (\pi/2\sqrt{3})\xi_0$, and $\lambda_L(0) = \sqrt{m/4\mu_0 n_s e^2}$. $\xi_0 = \hbar v_f/\pi\Delta$ is defined in the BCS theory, m is mass of elementary charge (e), and μ_0 is the vacuum permeability. Combining ξ_{GL} and λ_L, the ratio $\kappa = \lambda_L/\xi_{GL}$. The value of κ classifies superconductors into type I ($\kappa < 1/\sqrt{2}$) and type II ($\kappa > 1/\sqrt{2}$).

In an electromagnetic field, the supercurrent density $\vec{J}_s$ of a superconductor varies in both space and time as:

$$\vec{J}_s = -\frac{\Phi_0}{2\pi\mu_0\lambda_L^2}(\vec{\nabla}\theta + \frac{2\pi}{\Phi_0}\vec{A}) \tag{2.12}$$

where Φ_0 is the flux quantum, $\Phi_0 = h/2e$, $\vec{\nabla}$ is the gradient operator, and $\vec{A}$ is the vector potential. However, both θ and A are not physically measurable. Therefore, realizing a

[4] Gingzburg-Laudan theory well describes the electromagnetic properties of superconductors and predicts a distinction between type-I and type-II superconductors. Note that GL theory can also be derived from the microscopic BCS theory [44].

fixed relation between phase and vector potential, a gauge-invariant phase gradient γ is introduced:

$$\vec{\gamma} = \vec{\nabla}\theta + \frac{2\pi}{\Phi_0}\vec{A} \tag{2.13}$$

As a result, the expression of $\vec{J}_s$ is rewritten as:

$$\vec{J}_s = -\frac{\Phi_0}{2\pi\mu_0\lambda_L^2}\vec{\gamma} \tag{2.14}$$

indicating $\vec{J}_s$ scales with $\vec{\gamma}$ proportionally. By taking the curl of Eq. 2.12, with the Maxwell equation, we obtain:

$$\nabla^2\vec{B} = \frac{\vec{B}}{\lambda_L^2} \tag{2.15}$$

Solving Eq. 2.15 in one dimension gives $B = B_0 e^{-L/\lambda_L}$, which describes the external magnetic field to fall off exponentially inside a superconductor over λ_L, that is, the Meissner effect. Given that $\nabla \times B = \mu_0 J_s$, J_s also decays exponentially, as demonstrated in Fig. 2.3.

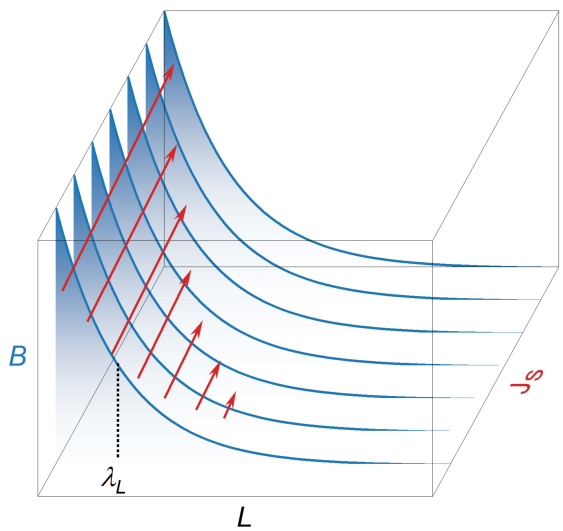

Figure 2.3: Illustrative representation of exponential decay of the applied magnetic field (B) and screening supercurrent density (J_s) from the surface over λ_L in a superconductor. B decays inside a superconductor and is ultimately screened, except for the thickness of the superconductor on the order of λ_L.

In addition, from the second London equation $\nabla \times (\mu_0 \vec{J}_s) = -\vec{B}/\lambda_L^2$ and Lorentz's law, we obtain the linearized form of the first London equation:

$$\frac{\partial \vec{J}_s}{\partial t} = \frac{\vec{E}}{\mu_0\lambda_L^2} \tag{2.16}$$

In a stationary state, $\vec{J}_s$ is constant in the superconductor (Eq. 2.16), so $\vec{E}$ is 0 and the supercurrent remains dissipationless.

2.3. Josephson Effects

2.3.1. Proximity effect

The Josephson effect is a manifestation of macroscopic quantum coherence in S/(weak link)/S hybrids. It was predicted theoretically by Brian D. Josephson and soon verified experimentally [46, 47]. In principle, the weak link can be an insulator (I) (as in the original work), a normal metal (N), a ferromagnet (F), but also for instance a constriction with a size smaller than ξ. When the weak link is an N layer between S layers and the interfaces are transparent, singlets can leak into the neighboring layer and exist over a characteristic coherence length. This is called the proximity effect. It means that the weak link with a thickness of the order of the characteristic coherence length becomes superconducting. As introduced before, singlets $|\uparrow\downarrow\rangle$ consist of opposite spins and can be accommodated in N metals. The characteristic coherence length in N is defined as:

$$\xi_N = \sqrt{\frac{\hbar D_N}{k_B T}} \tag{2.17}$$

where D_N is the N diffusion constant, on the condition of a diffusive regime ($\xi_N < l$, l the mean free path). ξ_N can be of the order of hundreds of nanometers in general (Fig. 2.4), depending on the amount of disorder and on temperature.

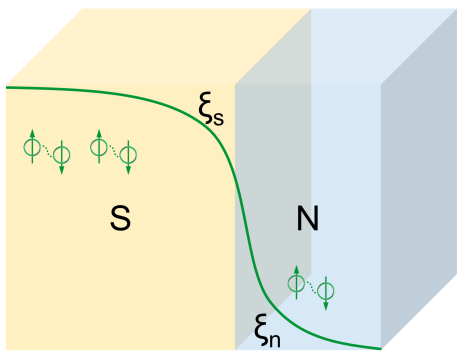

Figure 2.4: Depiction of the proximity effect in an S/N system. Singlets (green) can stay coherent up to hundreds of nanometers in N.

Knowing that singlet correlations can exist over substantial distances in N, an S/N/S hybrid can be a Josephson junction (JJ) device, as sketched in Fig. 2.5a. The supercon-

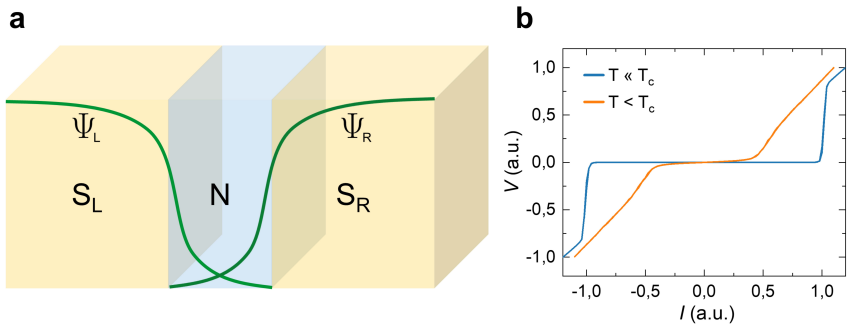

Figure 2.5: Sketch of an S/N/S Josephson junction. (a) Right and left S are weakly linked *via* the middle N layer, *i.e.* superconducting wave functions Ψ_L and Ψ_R overlap in N and stay coherent spatially (green curves). (b) I-V characteristic of the JJ clearly displays the zero-voltage state. Note the rounding feature of the IV curve (orange), which is due to phase slippage near T_c [48].

ducting wave functions (described by Eq. 2.9) overlap with each other in the N weak link and maintain coherence spatially, giving rise to Josephson coupling. We discuss the basic concepts of JJs below. Assuming the amplitude of Ψ is not changing in both right and left S electrodes, and representing γ (Eq. 2.14) by the gauge-invariant phase difference φ simple algebra gives:

$$J_s(\varphi) = J_c \sin(\varphi) \tag{2.18}$$

where $\varphi = \theta_L - \theta_R$. Eq. 2.18 describes the sinusoidal current-phase relation of a JJ. With an applied constant voltage, we obtain:

$$\frac{\partial \varphi}{\partial t} = \frac{2\pi}{\Phi_0} V \tag{2.19}$$

where Φ_0 is the flux quantum. This is the voltage-phase relation of a JJ. Solving Eq 2.19 yields linear a dependence of time on phase:

$$\varphi(t) = \varphi_0 + \frac{2\pi}{\Phi_0} V t \tag{2.20}$$

From this, we can define the Josephson frequency as $f = V/\Phi_0$. Moreover, the Josephson coupling energy is:

$$E_j = \int_0^{t_0} IV dt = \frac{\Phi_0 I_c}{2\pi}(1 - \cos\varphi) = E_{j0}\cos\varphi \tag{2.21}$$

where I_c is the critical current and temperature-dependent. Biasing a JJ by flowing a I_{bias} results in a modulated E_j, that is described by a tilted washboard potential, as will be discussed later. Usually, I_c of a JJ is the order of μA. In this case, thermal fluctuation $k_B T$ is not negligible, leading to the rounding feature in IV curves and raising ambiguity in determining I_c (orange curve in Fig. 2.5b). According to the model proposed by

Vinay Ambegaokar and B. I. Halperin [49]:

$$V = \frac{2I_c R_n}{\gamma_0} \frac{e^{\pi\gamma_0 i} - 1}{e^{\pi\gamma_0 i}} \left\{ \int_0^{2\pi} e^{-\pi\gamma_0\varphi/2} I_0\left(\gamma_0 \sin\frac{\varphi}{2}\right) d\varphi \right\}^{-1} \tag{2.22}$$

where $\gamma_0 = \Phi_0 I_c/\pi k_B T = 2E_{j0}/k_B T$, $i = I/I_c$, R_n represents the normal resistance, I_0 is a modified Bessel function. We analyze the energy competition between Josephson coupling and thermal fluctuation numerically, as shown in Fig. 2.6. With decreasing

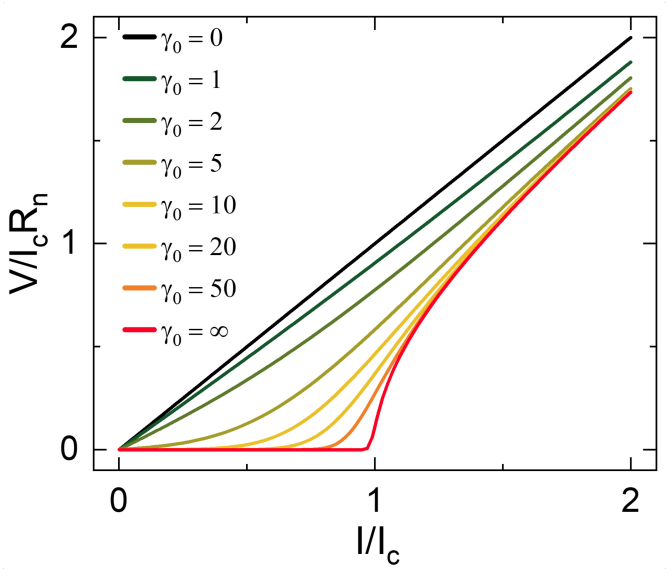

Figure 2.6: Numerical calculations of temperature-dependent Josephson coupling. As γ_0 increases, *i.e.* Josephson coupling becomes stronger at low temperatures, the rounding feature in the IV curve is significantly suppressed.

temperatures, I_c becomes larger, and correspondingly the rounding feature in the IV characteristic is significantly suppressed.

2.3.2. Macroscopic quantum coherence

The macroscopic quantum coherence of sustained by a JJ, *i.e.* Josephson coupling, manifests itself in a few interference effects. In the presence of a magnetic field, the Josephson coupling yields a superconducting quantum interference (SQI) pattern, in analogy to diffraction in optics, as displayed in Fig. 2.7. A magnetic field is applied along the z axis and decays in both right and left S electrodes over λ. In the case of the thickness of superconductor $t_s > \lambda$, the effective length of the N layer equals $d+\lambda_L+\lambda_R$. The total flux threading the JJ is hence defined as:

$$\Phi = \oint A d\ell = B(d + \lambda_L + \lambda_R)W \tag{2.23}$$

The variation of φ along the x axis is:

$$\frac{\partial \varphi}{\partial x} = \frac{2\pi}{\Phi_0} B(d + \lambda_L + \lambda_R) \tag{2.24}$$

Using Eq. 2.18 and solving Eq. 2.24, we obtain:

$$I_s = \int_{-W/2}^{W/2} \int_{-L/2}^{L/2} J_c \sin\left\{\frac{2\pi}{\Phi_0}(d + \lambda_L + \lambda_R)B + \varphi_0\right\} dz dx \tag{2.25}$$

The magnitude of I_s is field-dependent:

$$I_s(\Phi) = I_c \left| \frac{\sin \frac{\pi\Phi}{\Phi_0}}{\frac{\pi\Phi}{\Phi_0}} \right| \tag{2.26}$$

As demonstrated in Fig. 2.7b, the SQI pattern is Fraunhofer-like, with a central peak that has twice the width of the side lobes, and an amplitude of the side lobes following $1/B$. The Fraunhofer SQI pattern comes about when the current distribution over the weak link cross-section is homogeneous. Dynes and Fulton proposed a method to establish the spatial distribution of J_c from the SQI pattern [50]. This method has been adopted to scrutinize the superconducting junctions extensively and will be used for the analyses of the data in Chapter 5 [51–53]. It should also be noted that the period (ΔB) of the SQI pattern is dimension-dependent. The above discussion is based on the condition of $t_s > \lambda$. Once $t_s < \lambda$, the S electrode is in a 2D limit. As a consequence, the non-local electrodynamic effect has to be considered, instead of the Meissner effect [54–57]. In particular, in the limits of $L \gg W$ and $L \ll W$, R. Fermi, *et al.* found $\Delta B = 1.842\Phi_0/W^2$ and $\Delta B = 2\Phi_0/(LW)$. respectively [52]. This conclusion sheds light on understanding the SQI patterns obtained on long JJs, as discussed in Chapter 5 and Chapter 6.

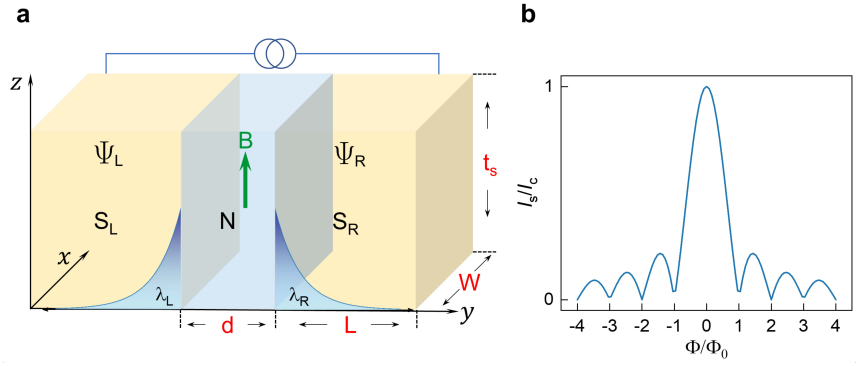

Figure 2.7: (a) Sketch of a JJ. d is the length of the JJ. W is the width of S, and L is the length. t_s is the thickness of S. The external field is applied along the z axis and current flows along the y axis. The field penetrates into the S layers and decays exponentially over the London penetration depth. (b) The Fraunhofer-like SQI pattern of a JJ. The central peak is two times wider, and the side lobes decay as $1/B$.

Additionally, according to Eq. 2.18 and Eq. 2.20, JJ has different responses to dc and ac voltage sources. If JJ is driven by a dc voltage, the time-averaged J_s is zero since the phase difference φ has a linear dependence on time. However, when an ac voltage is applied to the JJ, the situation changes completely. We define an ac voltage as:

$$V(t) = V_{dc} + V_1 \cos(\omega_1 t) \tag{2.27}$$

With the voltage-phase relation (Eq. 2.20) , we obtain:

$$\varphi(t) = \frac{2\pi V_1}{\Phi_0 \omega_1} \sin\omega_1 t + \frac{2\pi}{\Phi_0} V_{dc} t + \varphi_0 \tag{2.28}$$

Interestingly, inserting Eq. 2.28 in Eq. 2.18 and rewriting as Fourier series with the fact that $\mathscr{F}_{-n}(t) = (-1)^n \mathscr{F}_n(t)$ gives:

$$I_s(t) = I_c \sum_{n=-\infty}^{\infty} (-1)^n \mathscr{F}_n(\frac{2\pi V_1}{\Phi_0 \omega_1}) \sin[(\omega_{dc} - n\omega_1)t + \varphi_0] \tag{2.29}$$

From Eq. 2.29, we see quantized dc voltages appear in the JJ driven by an ac voltage. When the sine argument becomes zero periodically at $V_{dc} = n\Phi_0\omega_1/2\pi$, which corresponds to phase-locking states, quantized steps arise in the IV characteristics of the JJ, so-called Shapiro steps [58]. Qualitatively, in the framework of the tilted washboard potential ($E_j = E_{j0}[\cos\varphi - I_s\varphi/I_c]$), the motion of the phase ball can account for the appearance of Shapiro steps. Sweeping I_{dc} gives two states for the phase ball: (1) $I_{dc} + I_1 < I_c$, the phase ball is trapped in the well of the tilted washboard potential, and as soon as (2) $I_{dc} + I_1 > I_c$, the phase ball escapes from the local minimum and moves to the adjacent one in the tilted washboard potential. Consequently, at the values of $V_{dc} = n\Phi_0\omega_1/2\pi$, the phase ball moves synchronously with the ac source and crosses a certain number of minima in the tilted washboard potential for each cycle, concomitant with a phase change $\Delta\varphi = n\omega_1$. The appearance of Shapiro steps is the other indication of Josephson coupling in JJ, in addition to the SQI pattern.

Knowing the performance of a single JJ, the next relevant device is a superconducting quantum interference device (SQUID) consisting of two JJs, in which their wave functions interfere with each other (Fig. 2.8a). Therefore, in case of equal I_c in both JJ_1 and JJ_2, the total supercurrent is:

$$I_s = I_c \sin(\varphi_1) + I_c \sin(\varphi_2) \tag{2.30}$$

With $\varphi_1 - \varphi_2 = 2\pi\Phi/\Phi_0$, under the action of a magnetic field, the maximum of Eq. 2.30 is calculated as:

$$I_s(\Phi) = 2I_c \cos\left(\frac{\pi\Phi}{\Phi_0}\right) \tag{2.31}$$

As shown in Fig. 2.8b, the theoretical SQI pattern of a SQUID has equal-period lobes. Note the side lobes decay far more gradually than $1/B$ in experiment, even though field destroys superconductivity. We would like to point out a SQUID pattern can also be observed in a single JJ, where supercurrents flow in two channels, *i.e.* rim supercurrents, as seen in Chapter 5.

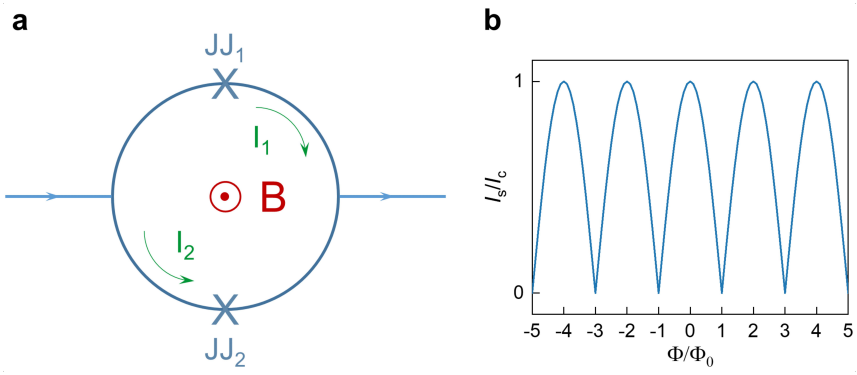

Figure 2.8: (a) Sketch of a SQUID, consisting of two JJs. A field is applied along the out-of-plane direction. (b) The theoretical SQI pattern of a SQUID. The wave functions of JJ_1 and JJ_2 interfere with each other, giving rise to a standard SQUID pattern with equal-period lobes. Note the side lobes do decay subject to field experimentally, but far more gradually than $1/B$.

2.3.3. Ferromagnetic Josephson junctions

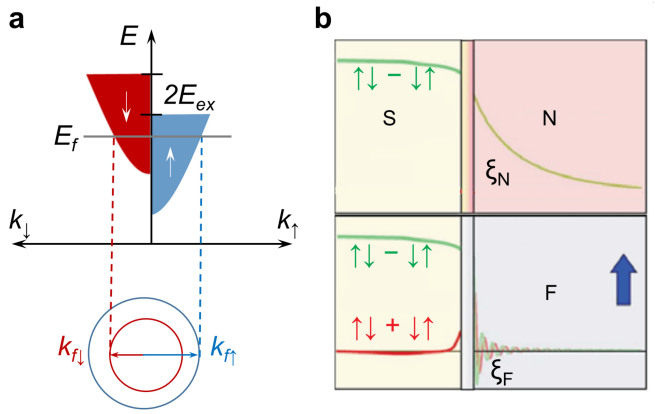

Figure 2.9: Depiction of the proximity effect in an S/F system. (a) The spin bands are shifted up ($k_\downarrow$) and down ($k_\uparrow$) by the exchange field, giving rise to Cooper pairs with non-zero center-of-mass momentum. (b) Top: Singlets (green) can stay coherent up to hundreds of nanometers in N. Bottom: Both singlets ($S = 0$ and triplets ($S_z = 0$) annihilate within several nanometers in F, exhibiting the SRP effect. Images adapted from Ref. [59].

A ferromagnet has a spin-split band structure with unequal spin subbands (Fig. 2.9a). The exchange field E_{ex} shifts the momenta of electrons at the Fermi level by $\pm\mathbf{Q}/2$ with $Q = 2E_{ex}/(\hbar v_f)$ in the diffusive limit, where v_f is the Fermi velocity. As a result, a finite momentum for $|\uparrow\downarrow\rangle$ is $k_{f\uparrow} - k_{f\downarrow} = \mathbf{Q}$, and for $|\downarrow\uparrow\rangle$ is $k_{f\downarrow} - k_{f\uparrow} = -\mathbf{Q}$. Singlets populating the Fermi level of F gain non-zero center-of-mass momentum, giving rise

to a spin-mixing state:

$$(\,|\uparrow\downarrow\rangle - |\downarrow\uparrow\rangle\,)\cos(\mathbf{R},\mathbf{Q}) + i(\,|\uparrow\downarrow\rangle + |\downarrow\uparrow\rangle\,)\sin(\mathbf{R},\mathbf{Q}) \tag{2.32}$$

The first term in Eq. 2.32 represents the spin-zero singlets, and the second term describes the exotic triplet correlations. Notably, the triplet correlations $|\uparrow\downarrow + \downarrow\uparrow\rangle$ have zero spin projection ($S_z = 0$) along the quantization axis of F and are thus subject to a short-range proximity (SRP) effect. This type of triplet correlation is the main source of equal-spin triplet ($S_z \neq 0$), which will be discussed later. The decoherence length ξ_F of the singlet-triplet mixture equals:

$$\xi_F = \sqrt{\frac{\hbar D_F}{E_{ex}}} \tag{2.33}$$

within the diffusive limit. E_{ex} is the order of eV, three orders of magnitude larger than $k_B T$. Therefore, the correlations of singlet and zero-spin triplet can only stay coherent within a length of 5 nm in conventional F like Co, Ni, *etc.* [11, 60], as shown in Fig. 2.9b. With increasing E_{ex}, ξ_F is even smaller than 1~2 nm. Note that the oscillating dependence of the singlet and triplet correlations on the junction length is due to a phase shift ($\pm\theta$) for $|\uparrow\downarrow\rangle$ and $|\downarrow\uparrow\rangle$, respectively. Different spins that are scattered by the exchange field at the spin-active interface get phase delays, as expressed by:

$$|\uparrow\downarrow\rangle e^{i\theta} - |\downarrow\uparrow\rangle e^{-i\theta} = (|\uparrow\downarrow\rangle - |\downarrow\uparrow\rangle)\cos(\theta) + i(|\uparrow\downarrow\rangle + |\downarrow\uparrow\rangle)\sin(\theta) \tag{2.34}$$

As a result, the interesting phenomenon of a $0-\pi$ transition can be realized by either varying the thickness of the F layer or changing the temperature of the junction, which has been extensively studied [60, 61].

So far, we have seen that superconductivity can be induced in spin-polarized F with a thickness of several nanometers. Such a length scale limits the practical application in the S/F systems. However, by rotating the quantization axis of the correlations with zero spin projection (Eq. 2.34), it should be possible to create other (equal spin) types of triplet correlations. Such equal spin triplets are not broken up by the ferromagnet.

Rotating the quantization axis can be done by having stacked S/F'/F hybrids where the magnetization in F and F' are non-collinear, as shown in Fig. 2.10. Note that the thickness of the F' layer should be smaller than $\xi_{F'}$. For simplicity, we consider the case of $\mathbf{M}'_F \perp \mathbf{M}_F$, *i.e.* $\mathbf{M}'_F$ points to the x direction, and $\mathbf{M}_F$ is aligned with the z axis. This is equivalent to a rotating magnetization from F' to F. What happens is that the spin mixing correlations in S still have a zero projection along the x axis. However, along the quantization axis of the F layer (z axis), triplets have non-zero components $|\uparrow\uparrow\rangle_z$ ($S_z = 1$) and $|\downarrow\downarrow\rangle_z$ ($S_z = -1$). These triplets ($S_z = \pm 1$) can stay coherent in the F layer over:

$$\xi_F = \sqrt{\frac{\hbar D_F}{k_B T}} \tag{2.35}$$

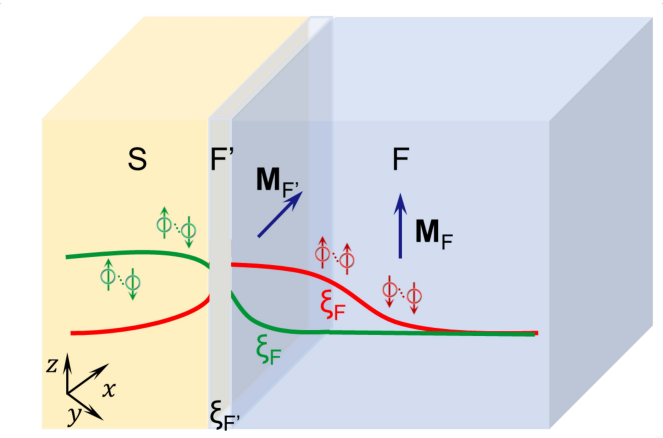

Figure 2.10: Schematic illustration of the LRP effect in stacked S/F'/F hybrids. The singlet to triplet conversion is optimized by setting $\mathbf{M}_{F'} \perp \mathbf{M}_F$. The generated triplets ($S_z = \pm 1$) can maintain coherent up to tens of nanometers in F.

This is the long-range proximity (LRP) effect. ξ_F is usually about tens of nanometers in conventional ferromagnets, depending on the spin diffusion length. Experimentally, the LRP effect has been observed in stacked multilayers of F with different orientations of spontaneous magnetization [62, 63]. Moreover, external magnetic fields enable setting up the magnetization either non-collinear or collinear, resulting in the creation and annihilation of the long-range triplet correlations [64].

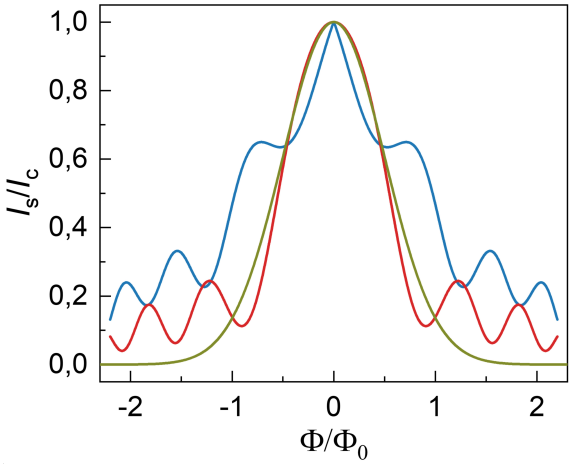

Figure 2.11: Representative abnormal SQI patterns of ferromagnetic JJ. The Blue and red curves are a result of the distribution of J_s in magnetized and demagnetized regions. The yellow curve is Gaussian-like, arising from the diffusive transport in the presence of disorder in JJ.

The macroscopic phase coherence of a ferromagnetic JJ can be distinguished from a normal JJ. Due to the additional parameter of an intrinsic magnetic flux, from the experimental point of view, J_c may be not spatially homogeneous in the ferromagnetic JJ. The magnetic flux, local barriers, and disorder can all affect the SQI pattern significantly [65–67]. Fig. 2.11 gives some examples of patterns that can occur due to magnetic non-uniformity, *i.e.* magnetic susceptibility depends on position and field. Taking into consideration the magnetic non-uniformity, the SQI patterns of a ferromagnetic JJ are abnormal, *i.e.* minima are non-zero, and the period of the side lobes varies, arising from an interference effect between magnetized and demagnetized areas. When JJ is in the diffusive regime, quasiparticles transport in random paths. Therefore, the SQI pattern is a result of interference of varying shapes, leading to a Gaussian-like pattern [68].

2.3.4. Half-metallic Josephson junctions

The LRP effect holds promise for practical applications in superconducting spintronics, in which magnetic orders and superconductivity can be operated interdependently [10, 11, 59]. Especially, in half-metallic ferromagnets (HMF; one spin band is conducting while the other is empty and far above the Fermi level), only one of the triplet correlations is allowed, *i.e.* $|\uparrow\uparrow\rangle$ ($S_z = 1$) or $|\downarrow\downarrow\rangle$ ($S_z = -1$). Consequently, the expectation is that spin-flip events are virtually absent so that the characteristic coherence length of HMF (ξ_{HMF}) can be hundreds of nanometers to even the micrometer scale [14, 69–71]. Note that, although triplet correlations are immune to exchange field in the HMF, they are not free of spin-orbit coupling [21].

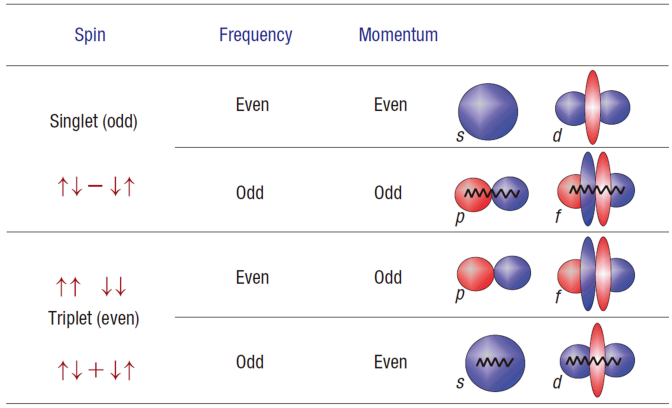

Figure 2.12: The four possible pairing symmetries subject to the Pauli exclusion principle. In a HMF, singlets cannot exist. The different components of triplet correlations, *i.e.* s, d, p, f waves stay in HMF, depending on the ballistic or diffusive regimes. Image adapted from Ref. [72].

The pending question is how to efficiently generate equal-spin triplet correlations in a HMF. LRP effects have been studied in CrO_2-based junctions [69, 70]. The triplet generator in such systems was believed to be intrinsic magnetic inhomogeneity of CrO_2 arising from either strain or boundary disorder. Also, triplets were found in manganite oxides $La_{0.7}Ca_{0.3}MnO_3$ (LCMO) and $La_{0.7}Sr_{0.3}MnO_3$ (LSMO) in combination with the high-T_c superconductor (HTS) $YBa_2Cu_3O_7$ [14, 73]. Visani, *et al.* demonstrated the transport of supercurrent in LCMO over a distance up to 30 nm and discussed the interfacial spin interference, verifying the occurrence of equal-spin Andreev reflectivity and triplets generation [73]. Very recently, a breakthrough on LRP effects was made in lateral YBCO/LSMO/YBCO junctions. Sanchez-Manzano, *et al.* reported a micrometer-scale transport of triplets in such a system at quite high temperatures [14]. However, the mechanism of triplets generation in manganite oxides is still not clear, in particular because no source of magnetic inhomogeneity was identified to act as triplet generator. This motivates the study of triplets in LSMO-based junctions in this thesis.

Intriguingly, in addition to the increasing I_c as temperature decreases, Eschrig, *et al.* predicted that I_c versus T of a HMF JJ should show a peak followed by the decrease of I_c at low T [72]. The origin was specified as follows: in moderately disordered HMF, triplets correlations of odd-frequency (time) even-momentum (space) s wave and d wave, multiplied by even-frequency odd-momentum p and f waves, mainly carry the supercurrent (Fig. 2.12). In the diffusive regime, s and p waves dominatd. It is well known s-wave triplet correlations are robust against disorders and impurities, *i.e.* scattering. Other components however are sensitive to scattering as they are anisotropic. Therefore, s-wave triplet correlations are believed to be the main source of supercurrent in HMF generally. However, as the temperature goes down, the p-wave component becomes pronounced, for example, in the diffusive regime. Experimentally, I_c was found to be quite high (up to mA) in HMF JJs based on CrO_2 [74]. In this thesis, we study LSMO-based JJs and will encounter scenarios both for the clean and for the diffusive regimes.[5] More discussions can be found in Chapter 5.

2.4. Experimental Methods

2.4.1. Sample fabrication

$La_{0.7}Sr_{0.3}MnO_3$ (LSMO) thin films are grown on (001)-oriented $(LaAlO_3)_{0.3}(Sr_2TaAlO_6)_{0.7}$ (LSAT) crystal substrates with a miscut angle of 0.15~0.2^o in an off-axis sputtering system. The deposition temperature is 700 ^oC, and the

[5] $I_c(T)$ peaks at low T both in the diffusive and clean limits, as predicted in Ref. [72, 75], but experimentally this has never yet been observed.

deposition pressure is kept at 0.7 mbar by using a dynamic butterfly valve and flowing a mixture gas of argon and oxygen (3:2). The sputtering power is 50 W. Subsequent to obtaining the required thickness of LSMO thin films (varying from 10 nm to 40 nm depending on the purposes of our projects), the system is cooled down to 25 ^oC at a rate of 10 ^oC/min. Thanks to the small lattice mismatch (-0.2%), LSMO thin films exhibit quite homogeneous electrical and ferromagnetic properties, which will be discussed in the section below. For the growth of bilayer NbTi/LSMO and trilayer NbTi/Ag/LSMO, NbTi and Ag layers are deposited $in\ situ$ at room temperature in a pure argon atmosphere, in order to get transparent interface. We would like to point out transparent interfaces are crucial for triplets generation, as demonstrated in Chapter 5 and Chapter 6.

To investigate both domain wall and non-local spin transport in the LSMO-based junctions (Chapter 3 and Chapter 4), LSMO thin films are patterned first with the help of electron beam lithography and ion beam etching. Then, electrical contacts (Pt or Ag) are made on the LSMO nanostructures with an electron beam resist mask, in a radio-frequency sputtering system. For the study of the LRP effect in the NbTi/LSMO hybrids, we structure the bilayer using an accurately designed Pt mask. The Pt mask is quite robust against ion beam etching. Moreover, the ion contamination coming from either ion beam etching or focused ion beam lithography can be prevented to a large degree by the capping Pt mask.

2.4.2. Characterization of the LSMO films

The epitaxy of LSMO thin films is examined using various characterization methods. As shown in Fig. 2.13a, atomic force microscopy (AFM) is utilized to map the morphology of a 20 nm LSMO thin film. We see clearly terraced surface without distinct inhomogeneity. The high-quality epitaxy of the LSMO thin film on the LSAT substrate is confirmed by x-ray diffraction (XRD) characterization, in which many side fringes are observed as a sign of the ideal epitaxy (Fig. 2.13b). Moreover, the temperature-dependent resistivity of the LSMO thin film was measured using a Van der Pauw method in a four-probe configuration. We use Al wires to connect the LSMO thin film to the circuit board electrically. To avoid the oxidation of the Al wires in contact with the LSMO thin film, Au pads are used as a buffer layer. The resistivity versus temperature measurement is performed in a Physical Property Measurement System (PPMS) from 400 K to 10 K. The resistivity is calculated based on $\rho = Rlt/l = Rt$, where l is the side length, t is the thickness of the LSMO thin film, and R is the measured sheet resistance. The Curie temperature (T_c) is determined to be 364 K from the inset $\mathrm{d}\rho/\mathrm{d}T$ curve (Fig. 2.13c). In addition, the saturation magnetization of the LSMO thin film is measured at 50 K using a magnetometer based on superconducting quantum interferometry and calculated to be 3.8 $\mu_B/f.u.$, in good agreement with the theoretical value. Therefore, we conclude

the LSMO thin film has no magnetically dead layer at the interface with the substrate [37].

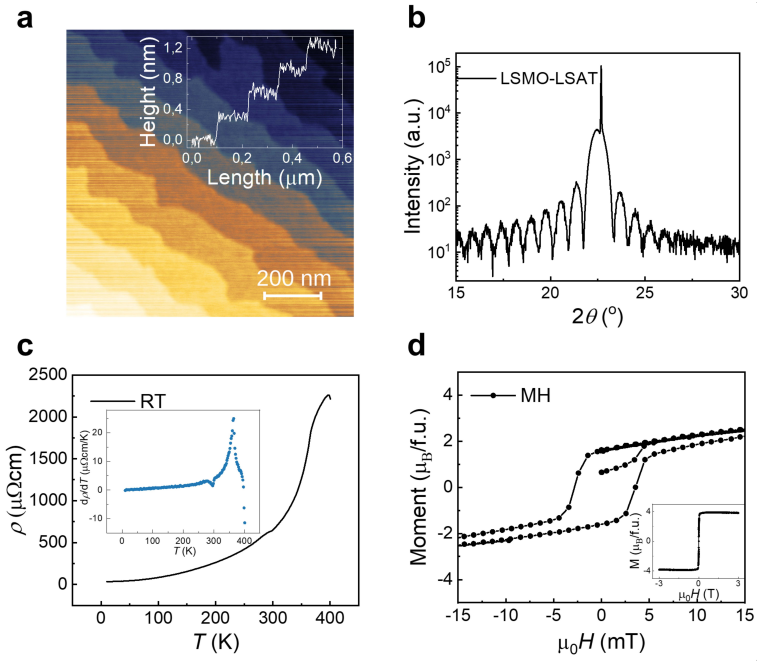

Figure 2.13: Characterization of the growth of a 20 nm LSMO thin film. (a) AFM image showing the terraced structure of the film, presumably following the substrate terraces. Inset is the line scan, demonstrating the step height is about 0.39 nm. (b) XRD measurement (intensity versus 2θ; θ is the beam angle of incidence), used to verify the epitaxial growth of the LSMO film on an LSAT substrate; side fringes are seen, but no undesired peaks of impurity phases. (c) A plot of the temperature-dependent resistivity $\rho(T)$. Inset: $\mathrm{d}\rho/\mathrm{d}T$ curve versus T. The Curie temperature of the LSMO thin film is determined to be 364 K. (d) Magnetization M versus applied magnetic field measured at 50 K. The saturated magnetization is calculated to be 3.8 $\mu_B/f.u.$, in agreement with the theoretical value.

Knowing the epitaxial LSMO thin film is of high quality, we study the spin transport in the normal-state LSMO nanostructures, *i.e.* DW and non-local spin transport. These two projects are carried out in the PPMS, which can change the temperature from 400 K to 10 K and offers fields up to 9 T both in plane and out of plane. Prior to performing the magnetoresistance measurements, a 1 T (-1 T) field is always applied to magnetize the LSMO nanostructures. Then, the magnetoresistance is recorded by flowing a dc current and sweeping the field from positive (negative) to negative (positive). More details can be found in Chapter 3 and Chapter 4. For investigating the spin transport in the superconducting LSMO nanostructures, *i.e.* generation and behavior of triplet correlations, a cryostat equipped with a vector magnet (Oxford Instrument) is used. A wide temperature range (from 300 K to 1.5 K) can be achieved, and a field up to 6 T can be obtained along a certain direction in this cryostat. Besides, a multi-channel lock-in de-

vice (Synktet MCL1-540) is programmed to take the data. The transport measurements in Chapter 5 and Chapter 6 are performed by applying an ac background current (~ 1 μA) and sweeping a superimposed dc current, and/or temperature to measure $R(T)$, $V(I)$ or$I_c(T)$ or $I_c(B)$ (SQI patterns) by sweeping the field. Also, a Heliox ^{3}He insert was employed to provide a base temperature of 300 mK for the study of the LRP effect in the long LSMO bars.

All the setups are programmed based on the SCPI language with Python through either GPIB or optical transmission. All the data in this thesis are processed and analyzed using standard Python packages.